2.C Limits on the Flux Limiter and Preheat from Analysis of Implosion Experiments with 1054-nm Illumination

Thermal electron transport plays an important role in the performance of direct-drive inertial-confinement-fusion targets. The laser energy absorbed in the corona is carried into the dense target through thermal electron transport and is converted into kinetic energy through the ablation process. The efficiency of the target drive and of the absorption of the laser light depend to a large extent on the efficiency of the thermal transport. In laser-fusion hydrodynamic codes the thermal transport is calculated with a diffusion model using Spitzer's model for thermal conductivity.[1] In the steep temperature gradients which exist in laser-fusion targets, the diffusion model with Spitzer's conductivity yields thermal fluxes larger than those available from the free-streaming electrons.[2] Code calculations, therefore, usually impose an upper limit on the conductivity given by some fraction of the free-streaming value, with the form $Q_f = fnkT(kT/m)^{1/2}$ where the parameter f, known as the flux limiter, is to be determined through experiments or from solutions to the Boltzmann equation.

The early experimental determinations of the flux limiter have concentrated mainly on planar targets (see Ref. 3 for a survey of the literature on the subject) while more recent efforts have focused on spherical targets. From the analysis of planar transport experiments carried out at LLE with 351-nm illumination, one concludes that both the thermal transport and the absorption could be modeled with f = 0.04.[4] Spherical experiments with 1054-nm illumination at the Rutherford Laboratory[5] could be described by uninhibited transport ($f \gtrsim 0.1$). Similar experiments at LLE provided a more complex picture.[6] In these experiments the transport was obtained from the measurement of the burn-through of the heat front through a plastic layer to an aluminum or titanium layer and from the mass-ablation rate calculated from ion collector traces. Conclusions from this experiment are listed below.

(1) The burn-through to the aluminum substrate was a factor of 2 to 3 larger than predicted by the code.

(2) The burn-through to the titanium substrate was well modeled, using a flux-limited value f = 0.05; the absorption fraction was also calculated properly under this condition.

(3) The mass-ablation rate obtained from the charge collectors was lower than that obtained from burn-through measurements. Simulation of the ablation rate from the charge collectors required $f < 0.1$.

To explain these results it was assumed that the heat front was not as steep as is expected from code calculations, but that a 200- to 300-eV foot precedes the front in the high-density material. Such a

foot would explain the large burn-throughs to the aluminum substrate but would not contribute to the ablation process. It would be produced by hot electrons (several times the thermal velocity) streaming from the hot corona into the cold, dense matter.

In this article we present the results of simulating implosion experiments which are sensitive to the flux limiter and preheat. Unlike the transport experiments described above, the transport in the implosion experiments is not measured directly; it is inferred from conditions in the target at stagnation which are sensitive to the transport and preheat.

A detailed analysis was carried out for shot 7035. Although there were many other shots in the series, this particular shot was chosen because the x-ray microscope images show most clearly the double-ring structure characteristic of the targets in this regime. Also, the focusing at 10 radii behind the target resulted in one of the most uniform implosions.

In shot 7035 a glass microballoon of 400-μm diameter and 1-μm thickness, filled with a 20-atm equimolar mixture of DT, was irradiated by 2.11 TW of 1054-nm laser light for 1.02 ns. The peak nominal irradiance was 7.9×10^{14} W/cm^2. Focusing with f/4 optics at a distance of 10 radii beyond the target center provided a uniform surface-illumination pattern. The target absorbed 709 J (0.33 absorption fraction) and the neutron yield was 1.5×10^{8}.

Simulation Conditions

The simulations for the uniform implosion shots were carried out with the laser-fusion design code *LILAC*. *LILAC* is a 1-D, Lagrangian hydrodynamic code that includes ray tracing of the laser light in the computation of the absorption, radiation transport with a diffusion approximation using LTE opacity tables, transport of the suprathermal electrons created by resonant absorption, and a post-processor which generates microscope and streak images.

The 2-D ray tracing was carried out with the azimuthally averaged, experimental, laser-intensity profile obtained at the equivalent target plane; similarly, the experimental focusing-optics parameters, f-number and focusing distance, were included. At the turning point the fraction of the absorbed energy due to resonant absorption was estimated using a formula from Kruer.[7]

The calculated absorption fraction of 0.30 agrees with the experimental value of 0.33. About 16% of the absorbed energy is accounted for by resonant absorption (corresponding to 5% of the incident energy). An *r*-*t* plot of the implosion is shown in Fig. 20.14 with a superimposed plot of the laser pulse. The results discussed below were obtained with a "legislated" absorption option in order to perform the parameter study over the flux limiter and preheat under the same absorption conditions. In this option the deposition into the suprathermal electron component is adjusted to maintain the resonance-absorbed fraction at prescribed levels (16% and 32%), and any energy not absorbed by either the inverse-bremsstrahlung or resonant processes is deposited in the thermal component at the critical surface.

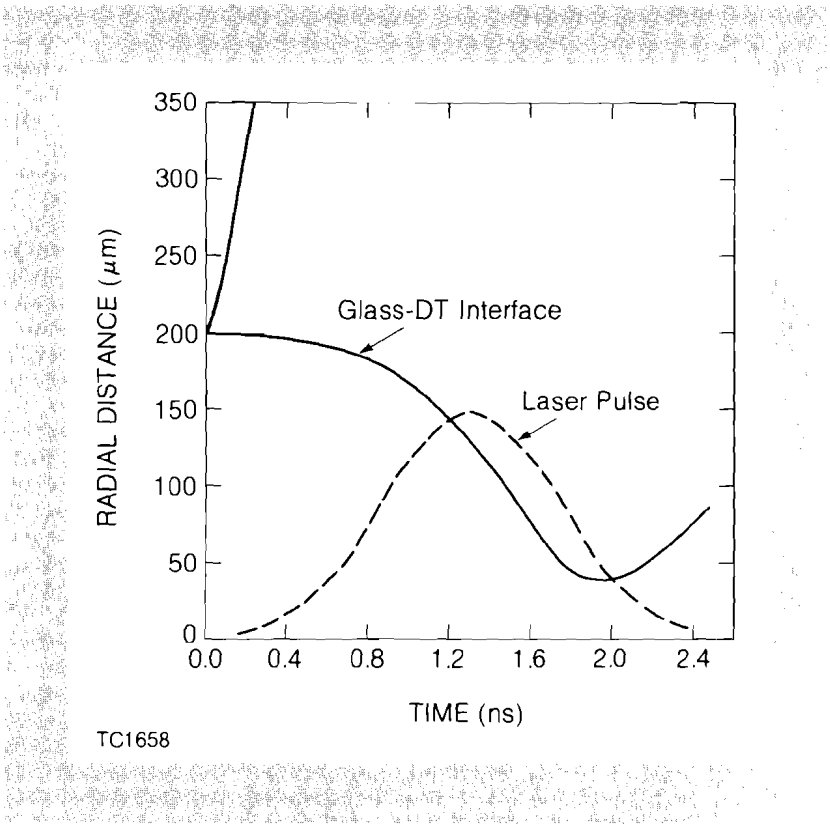

Fig. 20.14
Calculated trajectories of the outer surface of the target and of the glass-DT interface; the laser pulse is shown as a temporal reference.

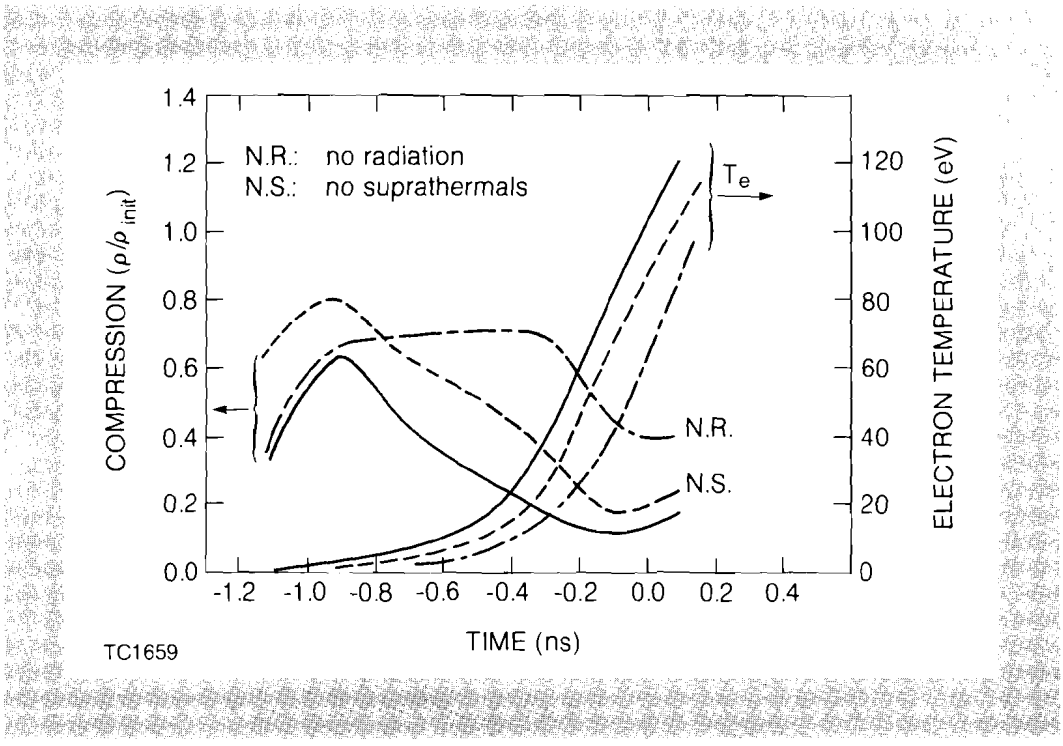

Fig. 20.15
Density and temperature in the pusher at a point initially 0.15 μm from the glass-DT interface during the implosion. Conditions were also calculated for no radiation and no suprathermals and are plotted for reference.

The dynamics of the implosion are those of an ablatively driven, "puffed-up" pusher. About 1 ns before the peak of the pulse, the glass shell is decompressed to ~ 0.2-0.3 times solid density by preheat from the initial shock, suprathermal electrons, and x-ray radiation. Figure 20.15 shows the conditions in the pusher during the implosion before recompression, for a position initially 0.15 μm inside the glass-DT interface. Most of the preheat in the first nanosecond is provided by the suprathermal electrons and the x-ray radiation from the hot plasma near the critical surface and in the heat front; each mechanism contributes about equally to the initial preheat. As the implosion proceeds, the radiation acts as a continuous preheat source which causes the shell to decompress to about 0.1 times solid density. The suprathermal electrons contribute little to the preheat during that time, so suppressing them from the computation hardly affects the conditions in the pusher. Suppressing the x-ray preheat has a much greater effect. The effect of the suprathermal electrons on the final implosion conditions and on the microscope images will be discussed later.

That the pusher is ablatively driven can be seen from the existence of an ablation front which progresses through the pusher. Figure 20.16 shows the electron temperature, mass density, and pressure profile in the pusher at one time during the implosion, 500 ps before the peak of the pulse. A typical ablation front has been set up with the pressure

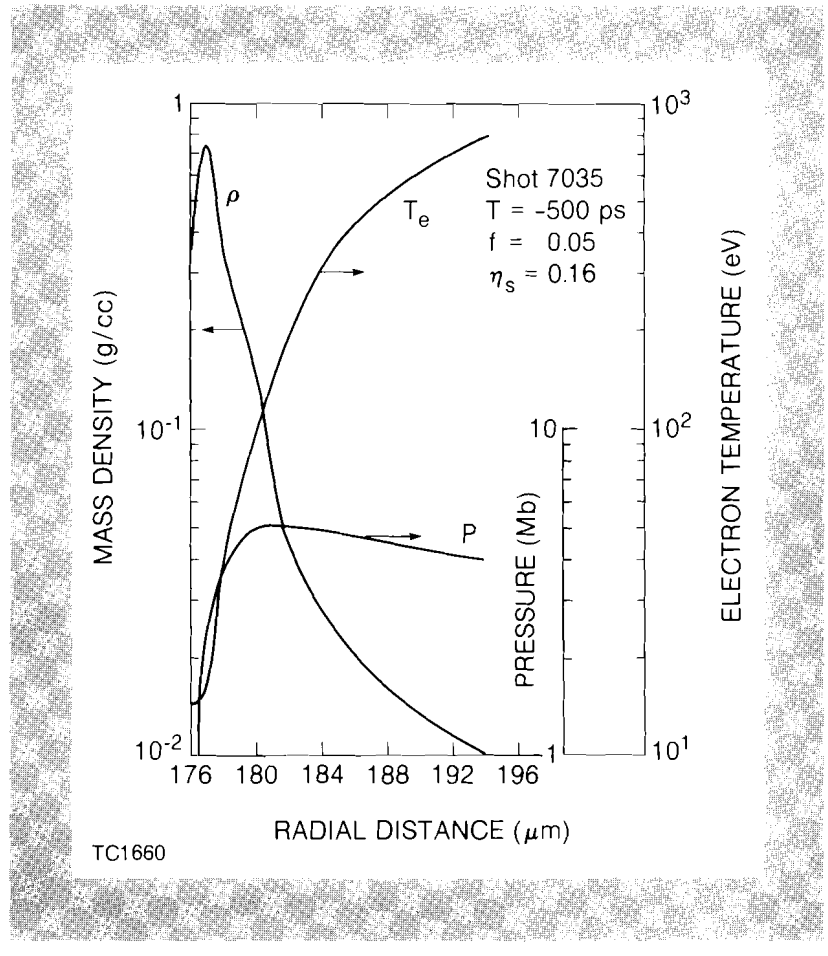

Fig. 20.16
Temperature, pressure, and density in the ablation region 500 ps before the peak of the pulse.

peak situated between the density and the temperature maxima. Other characteristics of the implosion, such as the progression of the ablation front through the pusher and the continuous ablation of target mass, indicate that the target is driven ablatively rather than explosively.

As the implosion proceeds, the pusher creates a shock wave in the fuel which preheats the fuel; this preheat is less than that in exploding pusher implosions because the pusher velocity increases more gradually. The pusher reaches a peak velocity of 2.4×10^7 cm/s. The shock wave reaches the center of the target about 90 ps after the peak of the pulse. The shock convergence and reflection raise the ion temperature in the central part of the fuel to several kilovolts and cause a neutron "burst" which lasts about 5 ps and produces about 1.2×10^9 neutrons. After shock reflection the pusher compresses the fuel to a peak density of 0.8 g/cc (four times that of liquid DT) with ion temperatures ranging from 0.4 keV near the pusher wall to 1.6 keV in the center. The compression phase produces another neutron burst of roughly the same magnitude as the previous one; the total neutron yield is 2.2×10^9 and the neutron-averaged ρR attains a maximum of 0.001 g/cm.

The experimental neutron yield was 1.8×10^8. A double burst of neutrons like that in the code simulation has been observed indirectly in measurements of the proton spectrum with a time-of-flight spectrometer by a group from the University of Illinois in similar experiments on the OMEGA laser system.[8] Both the measurements and the simulation with *LILAC* show a double-peaked proton spectrum which can be related to a double-peaked neutron production. A double-peaked proton spectrum is produced when conditions in the tamper, where the protons are primarily slowed down, are different for each neutron burst. Therefore, although the neutron yield of the simulation exceeds the experimental yield by about a factor of 10, not all the yield can be attributed to shock heating; a fraction of the experimental yield results from compression of the fuel by the glass pusher after shock reflection. Such compression heating requires reasonably good pusher symmetry during the implosion and stagnation. The lower experimental neutron yield is probably the result of lower temperatures during shock convergence because of imperfect spherical conditions. Such conditions may be due to non-uniformity in illumination and to the presence of the stalk. Lower shock-heating temperatures in the fuel lead to lower compression heating and, therefore, to a lower neutron yield.

The experimental x-ray microscope image and a scan of the film density along one diameter are shown in Fig. 20.17(a). The image shows a distinct bright outer ring surrounding a weaker ring and an inner structure which can be loosely interpreted as a bright inner ring. That weak/strong ring structure can also be observed in the scan. It also appears for two other combinations of filters. The microscope image obtained from the simulation is shown in Fig. 20.17(b) as a plot of the radial variation of x-ray intensity. The inner ring results from the x rays emitted from the inner surface of the glass pusher at stagnation. That surface is heated mostly by conduction from the DT fill and by the reflected shock. The outer ring is produced by the almost

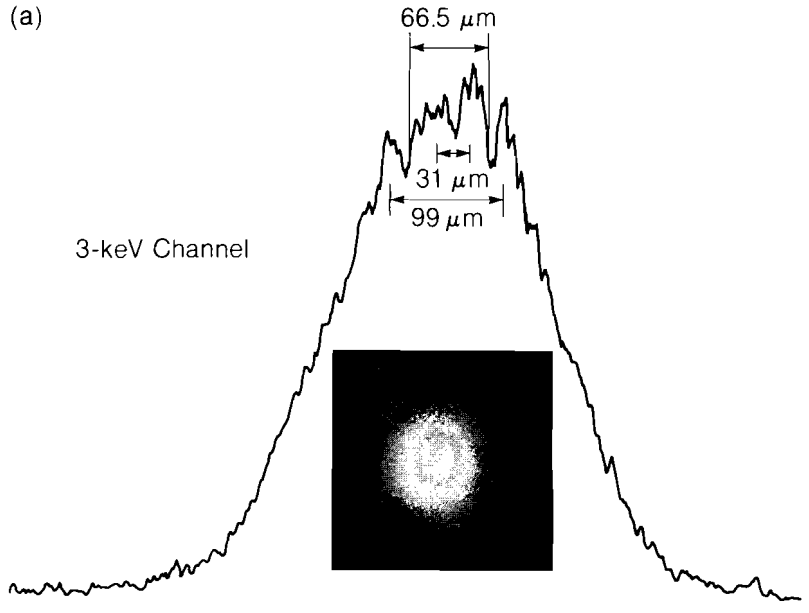

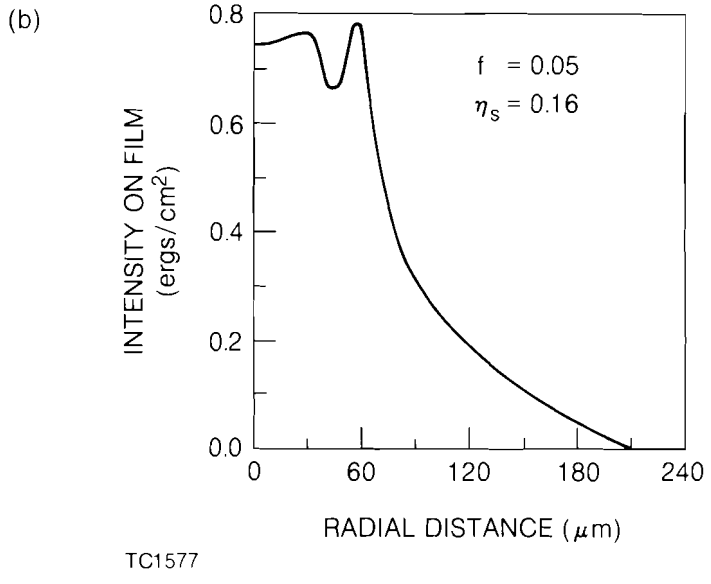

Fig. 20.17
X-ray microscope image for shot 7035: (a) experimental, (b) simulated.

stationary heat front when the pusher stagnates. The region from which the strong x-ray emission originates is narrow and corresponds to an optimum combination of electron temperature and density in the heat front. The integrated energy from that emission is usually small and does not show up in microscope images because the emitting

region moves continuously during the implosion. When the pusher stagnates, the density of the pusher increases slightly and the emitting region remains stationary long enough to produce a ring in the microscope image. Figure 20.18 plots the spatial distribution of x-ray emission from the pusher at various times near stagnation. Early in time, before stagnation, only the ring structure associated with the heat front can be seen. At stagnation the inner surface of the glass also becomes stationary and more dense and dominates the streak image. A short time later, it has cooled and again the ring associated with the heat front, which is still hot, dominates the image. The integration of these streak images over time leads to the double-ring microscope image observed in the experiment.

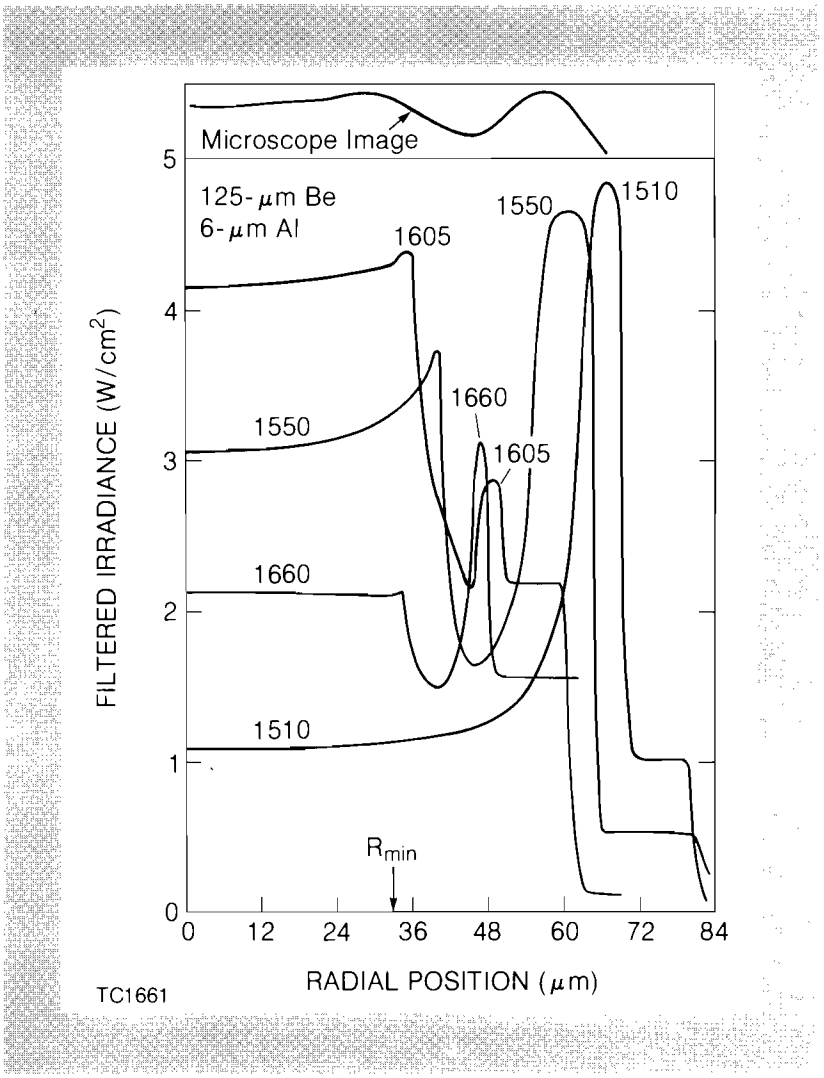

Fig. 20.18
Several frames of the x-ray emission from the target during stagnation. X-ray microscope images plotted above for reference.

The presence of the ring structure in the x-ray microscope images is sensitive to the two free parameters in the simulation: the flux limiter and the fraction of the absorbed energy that goes into the suprathermal electron component η_s. A caveat for the analysis is that the simulated microscope images are obtained from x-ray emission calculated from LTE (local thermal equilibrium) opacity tables. Non-LTE emission usually yields lower x-ray intensities because of the

ionization lag when the temperature increases rapidly. The effect may be more important in the production of the outer ring because the heat front moves rapidly through the cold glass. On the other hand, the material on the inner part of the glass is continuously heated to emission temperatures over a longer time and, therefore, may have a better chance to reach LTE conditions. Also, the code-calculated images are for the incident intensity on the film rather than for the film density; the film response will tend to reduce the apparent intensity differences in the core region, but not the shape, because of exposure saturation.

Figure 20.19 shows the x-ray microscope images calculated by *LILAC* for several values of f and η_s; the images are for a given filter combination (6 μm of Al and 125 μm of Be). Code results show that the greater the thickness of the Be foil, the higher the emission from the outer ring with respect to that of the inner core. The experimentally observed microscope images show the weak ring structure for all three filter combinations. Two general observations can be made. First, the larger the flux limiter, the weaker the outer ring emission is with respect to the inner core emission; second, the larger the absorbed energy in suprathermal electrons, the weaker the emission from the core structure.

The combinations of f and η_s which yield a weak ring between an outer emitting ring and a core structure are those of Figs. 20.19(b) and 20.19(d) in which f = 0.03 and 0.05, respectively, and η_s = 0.16. The ring in Fig. 20.19(c) is probably too weak to record photographically. The weak/strong ring structure does not exist for the other filter combinations. For the larger flux limiter, f = 0.08, the weak/strong ring structure does not exist; it is doubtful that non-LTE effects would lead to the experimentally observed structure since they would weaken an already inconsequential outer ring. In Fig. 20.19(a), no inner structure is seen; in this case the non-LTE effects could reduce the emission from the outer ring enough to let the inner core structure appear. For all values of the flux limiter, doubling the energy absorbed into the suprathermal electrons reduces the intensity of the inner ring to a point where it almost disappears.

Two conclusions can be drawn from the simulation. First, the flux limiter which provides the best description of implosion experiments is less than 0.08 and most likely larger than 0.03. This result agrees with those of the planar transport experiment at 351 nm and with the flux limiter required to model the burn-through to a titanium substrate in the spherical transport experiments at 1054 nm. Second, the fraction absorbed into the suprathermal electron component must be less than 20% of the total absorbed energy.

This places an upper limit on the preheat level in the pusher during the implosion. With η_s = 0.16 the glass is preheated to less than 100 eV during the implosion. This preheat level is much lower than that required in the spherical transport experiment to explain the large burn-through in plastic to the aluminum substrate, and other mechanisms must be sought to explain the aluminum emission.

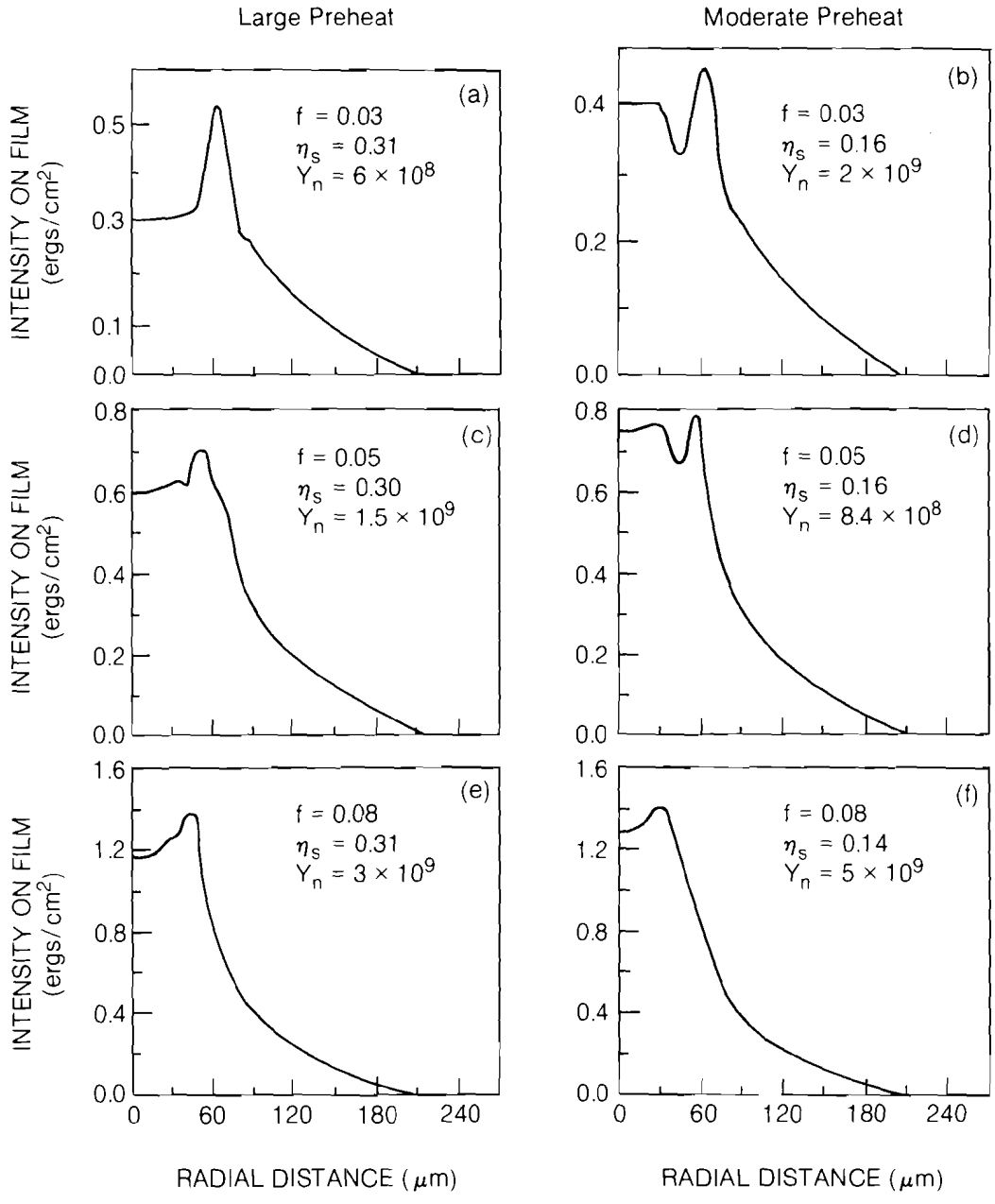

Fig. 20.19
X-ray microscope image for three values of the flux-limiter and two values of the absorbed energy in the suprathermal electron component.

ACKNOWLEDGMENT

This work was supported by the U.S. Department of Energy Office of Inertial Fusion under contract number DE-AC08-80DP40124 and by the Laser Fusion Feasibility Project at the Laboratory for Laser Energetics which has the following sponsors: Empire State Electric Energy Research Corporation, General Electric Company, New York State Energy Research and Development Authority, Northeast Utilities Service Company, Ontario Hydro, Southern California Edison Company, The Standard Oil Company, and University of Rochester. Such support does not imply endorsement of the content by any of the above parties.

REFERENCES

1. L. Spitzer and R. Harm, *Phys. Rev. Lett.* **89**, 977 (1953).
2. D. R. Gray and D. J. Kilkenny, *Plasma Phys.* **22**, 81 (1980).
3. W. C. Mead *et al.*, *Phys. Fluids* **27**, 1301 (1984).
4. B. Yaakobi, T. Boehly, P. Bourke, Y. Conturie, R. S. Craxton, J. Delettrez, J. M. Forsyth, R. D. Frankel, L. M. Goldman, R. L. McCrory, M. C. Richardson, W. Seka, D. Shvarts, and J. M. Soures, *Opt. Commun.* **39**, 175 (1981).
5. T. J. Goldstack *et al.*, *Phys. Fluids* **25**, 1634 (1982).
6. B. Yaakobi, J. Delettrez, L. M. Goldman, R. L. McCrory, R. Marjoribanks, M. C. Richardson, D. Shvarts, S. Skupsky, J. M. Soures, C. P. Verdon, D. M. Villeneuve, T. Boehly, R. Hutchison, and S. Letzring, *Phys. Fluids* **27**, 516 (1984).
7. W. L. Kruer, LLNL Report UCRL-81896 (1978).
8. D. R. Welch, D. B. Harris, A. H. Bennish, and G. H. Miley (pre-publication manuscript).